

Geometric segmentation of sea clutter in coherent radar images: Range-Doppler Map versus Range-Time Intensity Map

Jordan Michelet*, Laurent Mascarilla*, Henry Chandran,[†]*Member, IEEE*, and Michel Berthier* * Laboratory MIA, La Rochelle University 17000, France [†] Bowen Company, Les Ulis 91940, France

Abstract—This paper aims at providing an efficient algorithm for sea clutter segmentation in coherent radar images. Using multi-phase interface motion models, we show that segmentation in the Range-Time Intensity Map gives much more relevant results than segmentation in the Range-Doppler Map and avoids the use of assumptions on the clutter frequency response. Several mathematical models are evaluated on real data corresponding to *Douglas* sea states of approximately 5. Dealing with diffuse interface motion models involving more than two phases allows to take into account the low contrast, the interference noise, and the contour weakness that are typical of Range-Time Intensity Map images. Sea clutter segmentation allows for instance to obtain oceanographic parameters such as sea state, direction and velocity of the swell and the wind. It can also be seen as a pre-processing that may be useful for target detection.

Index Terms—Doppler Radar, Backscattered Energy, Sea Clutter, Segmentation, Range-Time Intensity map, Range-Doppler Map, Multi-Phase Interface Motion, High Sea States.

I. INTRODUCTION

SEA clutter or sea echo refers to the backscattered returns from a patch of the sea surface illuminated by a transmitted radar signal. It is usually assumed to be composed of slow clutter due to *Bragg* scattering of capillary waves and of fast clutter arising from gravity wave phenomena such as breaking waves [17]. Sea clutter segmentation allows for instance to obtain oceanographic parameters such as sea state, direction and velocity of the swell and the wind, [14]. It can also be seen as a pre-processing that may be useful for target detection.

Hitherto, sea clutter modeling is usually considered as a problem formulated in the Range-Doppler Map (RDM). Statistical distributions are designed that aim at describing, from the frequency viewpoint, the superposition of different kinds of waves aforementioned. The Doppler response of the sea clutter can occupy a fairly wide frequency band with very irregular contours, especially in the direction of the wind, *i.e.* in upwind (meteorological) conditions [5], [16].

One can address sea clutter segmentation by means of two-class classification algorithms [6], [9], [24]. Such algorithms aim at partitioning the RDM into two regions: the so-called exo-clutter, and endo-clutter regions. However, when dealing with real data, the spectral information intricacy makes it difficult to obtain reliable characteristics of the exo-clutter and endo-clutter regions. The probabilistic models involved are generally relevant only in very specific cases [22], [20], and, to the best of our knowledge, there is no model for arbitrary cases [21].

Alternatively, and because we are dealing with the only sea clutter, one can consider performing segmentation in the initial Range-Time Intensity (RTI) map, *i.e.* using the only reflectivity information given by non-coherent integration. Such approaches have already been investigated [18], [19], that also make use of assumptions about the nature of the sea clutter.

The main objective of this contribution is to propose a geometric algorithm for sea clutter segmentation that does not involve assumptions or models for the sea clutter. We investigate the performance of three segmentation processes based on multi-phase interface motion models [2], [7], [8], [10], [12], [13], [25] and applied first in the RDM and then in the RTI map. Experiments on real data show that the best results are obtained when the segmentation is performed in the RTI map with visualization in the RDM.

Our choice to use multi-phase interface motion models is motivated by the specific characteristics of the images namely low contrast, interference noise, and weak contours [16], [17], which make them difficult to process. We also take advantage of the fact that it is possible to segment the sea clutter using a number of phases large enough to manage its complexity.

Experiments are conducted on real data coming from the South African Council for Scientific and Industrial Research (CSIR) dataset [23] and corresponding to *Douglas* sea states about 5 with targets having tangential motion or positive Doppler frequencies.

The main contribution of this paper can thus be summarized as follows. By investigating several multi-phase interface motion models, we propose a simple, efficient, and unsupervised algorithm that allows to perform, in the RTI map, an accurate segmentation of the sea clutter, when visualized in the RDM.

The rest of this paper is organized as follows. Section II is devoted to the mathematical description of the three multi-phase interface motion models that are used for the experiments, namely the level-set sharp interface motion, the log-likelihood driven two-phase diffuse interface motion, and the Chan-Vese k -phase diffuse interface motion. In Section III, the methodology of the experiments is discussed and information on the used data are given. Then, the results of the segmentation obtained in the RDM, resp. in the RTI map, are presented in Section III-B, resp. in Section III-C. These results are discussed in Section III-D and the conclusion is in Section IV.

II. MOVING INTERFACE APPROACHES OF SEGMENTATION

THIS section is devoted to the mathematical description of the three methods that are used in the sequel to segment the sea clutter. These methods are geometric in nature and are essentially based on the dynamics of the mean curvature flow [11]. The goal is to obtain a contour by letting an interface evolve according to the dynamics given additional constraints. The first method is the level-set method [2], [7], [13], which is well-known to be a reference method with numerous possible applications. It produces a contour which is a sharp interface given by the evolution of the zero level-set of a function. This evolution essentially takes into account information, *e.g.* contour strength, in a neighborhood of the moving interface.

The second method makes use of a two-phase-field model, the *Allen-Cahn* model [1], driven by a log-likelihood ratio [12]. On the one hand, the produced interface of size ε is diffuse. It can be seen as a fuzzification of the contour to be detected. On the other hand, the log-likelihood ratio is computed between non-parametric estimates of the pixel distributions in each of the two phases. Hence, the resulting dynamics takes into account more global information.

The third method, which is also a phase-field model with a diffuse interface, allows to consider an arbitrary number of phases and is constrained by an adaptation of the *Chan-Vese* data attachment term [4], [8], [10], [25]. The main advantage is that it avoids reducing the segmentation problem to a two-class problem. It appears that the complexity of the images to be processed makes it difficult to give one, and only one, characteristic of the sea clutter. This approach, by gathering various information in multiple phases, is more adapted to our problem.

A. Level-set sharp interface motion

THIS method, introduced in [13], is one of the most popular methods of segmentation. The underlying idea is to handle an interface by making the zero level-set of a function evolve according to the mean curvature flow [11]:

$$\frac{\partial \phi}{\partial t} = |\nabla \phi| \operatorname{div} \left(\frac{\nabla \phi}{|\nabla \phi|} \right), \quad (1)$$

where $\operatorname{div}(\cdot)$ denotes the divergence. With additional constraints, the resulting scheme for the space-time function ϕ writes [7]:

$$\begin{aligned} \phi^{n+1} &= \phi^n + \Delta t \operatorname{div} (d_p(|\nabla \phi^n|) \nabla \phi^n) \quad (2) \\ &+ \Delta t \lambda g(\mathcal{I}) \delta_\varepsilon(\phi^n) \operatorname{div} \left[g(\mathcal{I}) \frac{\nabla \phi^n}{|\nabla \phi^n|} \right] + \Delta t \alpha g(\mathcal{I}) H_\varepsilon(-\phi^n), \quad (3) \end{aligned}$$

where $\mathcal{I}(x)$ is the intensity of the image at position x , Δt is the time step, ε is the size of the moving interface contour and g is an edge indicator function, for instance, given by:

$$g(x) = \frac{1}{1 + |\nabla (K_\sigma * x)|^2},$$

with

$$K_\sigma(x) = \frac{1}{\sigma \sqrt{2\pi}} e^{-\frac{x^2}{2\sigma^2}}, \quad (4)$$

the *Gaussian* kernel with standard deviation σ . The regularized analogs δ_ε and H_ε of *Dirac* and *Heaviside* distributions

(respectively weighted by the coefficient λ and α in (3)) are chosen to be

$$\begin{aligned} \delta_\varepsilon(x) &= \begin{cases} \frac{1 + \cos\left(\frac{\pi x}{\varepsilon}\right)}{2\varepsilon} & \text{if } |x| \leq \varepsilon, \\ 0 & \text{if } |x| > \varepsilon \end{cases}, \\ H_\varepsilon(x) &= \begin{cases} 0 & \text{if } x < -\varepsilon \\ \frac{1}{2} + \frac{x}{2\varepsilon} + \frac{1}{2\pi} \sin\left(\frac{\pi x}{\varepsilon}\right) & \text{if } |x| \leq \varepsilon. \\ 1 & \text{if } x > \varepsilon \end{cases}. \end{aligned}$$

The parameters of the level set scheme are: $\Delta t, \lambda, \alpha, \sigma$ and ε . The contour to be detected is given by $\phi = 0$. Part (2) of the scheme makes use of the first derivative d_p of the potential function p defined by [7]:

$$d_p(x) = \frac{p'(x)}{x}, p(x) = \begin{cases} \frac{1}{4\pi^2} (1 - \cos(2\pi x)) & \text{if } x \leq 1 \\ \frac{(x-1)^2}{2} & \text{if } x > 1 \end{cases}.$$

In addition to the mean curvature term weighted by the edge indicator, part (3) of the scheme involves a supplementary term intended to speed up the level-set evolution process. The function δ_ε used in (3) tends to confine the dynamic of the mean curvature flow in a small neighborhood of the moving interface. To initialize the algorithm, one usually chooses a contour surrounding the region to be segmented.

There are variants of the level set algorithm that can take into account a number $k > 2$ of phases. However, given the specificities of the images to be processed in our case, these variants are difficult to implement. Indeed, they require ad hoc reinitializations during the process in order to stabilize the algorithm. Our goal being to obtain an algorithm with as little supervision as possible, these variants are not considered in what follows.

B. Log-likelihood driven two-phase diffuse interface motion

THE *Allen-Cahn* reaction-diffusion equation, introduced in [1], aims at describing the dynamic of a system whose phase-field function evolves to take two different values, 0 and 1. Each of these values characterizes one region denoted by OUT and IN respectively. Contrary to the level set model, the produced interface is a diffuse interface of width ε in which the phase-field function varies smoothly from 0 to 1. *Allen-Cahn* equation,

$$\frac{\partial \phi(x, t)}{\partial t} = \varepsilon^2 \Delta \phi(x, t) - W'(\phi(x, t)), \quad (5)$$

is the L^2 -gradient descent of the *Cahn-Hilliard* energy,

$$E^{CH}(\phi) = \int_{\Omega} \left(W(\phi(x, t)) + \frac{\varepsilon^2}{2} |\nabla \phi(x, t)|^2 \right) dx, \quad (6)$$

where W is the double-well potential defined by:

$$W(x) = \frac{x^2(1-x)^2}{2}. \quad (7)$$

Remark 1: Let us denote $q(x) = \frac{1}{2}(1 - \tanh(\frac{x}{\varepsilon}))$ the profile function and d the signed distance to the moving interface Γ_t . Using the fact that d satisfies the eikonal equation

$$|\nabla d| = 1,$$

one can show that the mean curvature, defined in (1), applied to d implies that the function

$$\phi_\varepsilon(x, t) = q \left(\frac{d(x, \Gamma_t)}{\varepsilon} \right)$$

satisfies (5) (see for instance [3, p. 18]).

The dynamics of the Allen-Cahn equation is driven by the minimization of the log-likelihood ratio between estimates of the pixel intensity distributions in the regions IN and OUT of \mathcal{I} . In our setting, the log-likelihood ratio $LL(\cdot)$ between two pixel intensity distributions P_{IN} and P_{OUT} is given by

$$LL(P_{\text{IN}}, P_{\text{OUT}}) = -\log \left(\frac{\prod_{x \in \text{IN}} P_{\text{IN}}(\mathcal{I}(x)) \prod_{x \in \text{OUT}} P_{\text{OUT}}(\mathcal{I}(x))}{\prod_{x \in \text{IN} \cup \text{OUT}} P_{\text{IN} \cup \text{OUT}}(\mathcal{I}(x))} \right),$$

where $P_{\text{IN} \cup \text{OUT}}$ is the distribution of the null hypothesis followed by the pixel intensities in IN and OUT. For the computation of the gradient descent corresponding to this minimization problem, see [12]. In what follows, the distribution P_{IN} , resp. P_{OUT} , is given by the non-parametric Parzen estimator $\hat{f}_{h, \text{IN}}$, resp. $\hat{f}_{h, \text{OUT}}$.

To improve computational times, a multi-grid scheme based on a Lie splitting is used (for more details, see [12]). The Lie splitting allows to decompose the partial differential equation of the gradient descent into three sub-equations that can be solved exactly. Concretely, the main steps of the resulting multi-grid scheme are described in the following sections [12].

1) Minimization of the log-likelihood ratio:

$$\phi^n(\bar{x}) \leftarrow \left(\phi^n(\bar{x}) - \frac{T_{\text{IN}}}{T_{\text{OUT}}}(\bar{x}) \right) e^{T_{\text{OUT}}(\bar{x})\Delta t} + \frac{T_{\text{IN}}}{T_{\text{OUT}}}(\bar{x}),$$

where \bar{x} is a cell of size a and composed of a^2 pixels (induced by the multi-grid scheme), T_{IN} and T_{OUT} are defined by:

$$T_{\text{IN}}(\bar{x}) = 2a^2 \sum_{\mathcal{I}} \hat{f}_{h, \bar{x}}(\mathcal{I}) \ln [\hat{f}_{h, \text{IN}}(\mathcal{I}) \hat{f}_{h, \text{OUT}}(\mathcal{I})],$$

$$T_{\text{OUT}}(\bar{x}) = 2a^2 \sum_{\mathcal{I}} \hat{f}_{h, \bar{x}}(\mathcal{I}) \ln [\hat{f}_{h, \text{OUT}}(\mathcal{I})],$$

where the weighted Parzen estimator $\hat{f}_{h, E}$ is given by [15]:

$$\hat{f}_{h, E}(x) = \frac{1}{h \sum_{x_i \in E} \omega(x_i)} \sum_{x_i \in E} \omega(x_i) K_1 \left(\frac{x - x_i}{h} \right),$$

with $E = \text{IN}$ or $E = \text{OUT}$. We set $\omega = 1 - \phi^n$ if $E = \text{IN}$ and $\omega = \phi^n$ if $E = \text{OUT}$. The parameter h is the smoothness coefficient and K_1 is defined by (4) with $\sigma = 1$. More details about the relevance and the computation of these non-parametric estimates are given at the end of the subsection.

2) Effect of the reaction term of Allen-Cahn equation:

$$\phi^n \leftarrow \frac{1}{2} \mathcal{X}_{\{\phi^n = 1/2\}} + g_C^+ \mathcal{X}_{\{\phi^n > 1/2\}} + g_C^- \mathcal{X}_{\{\phi^n < 1/2\}},$$

where the functions g_C^+ and g_C^- are given by:

$$g_C^+ = \frac{\sqrt{1+4C} + 1}{2\sqrt{1+4C}}, \quad g_C^- = 1 - g_C^+,$$

with

$$C = \phi^n \frac{1 - \phi^n}{(1 - 2\phi^n)^2} e^{-\frac{\alpha a^2 \Delta t}{\varepsilon c_W}},$$

α being a regularization parameter, ε the width of the interface, and c_W the constant

$$c_W = \int_0^1 W(x) dx.$$

3) Effect of the diffusion term of Allen-Cahn equation:

$$\phi^{n+1} = \mathcal{F}^{-1} \left\{ G(k) \mathcal{F} \{ \phi^n \} (k) \right\},$$

where \mathcal{F} , resp. \mathcal{F}^{-1} , denotes the Fourier transform, resp. the inverse Fourier transform, k is the Fourier variable, and

$$G(k) = \exp \left(-4\pi^2 \frac{\varepsilon \alpha}{c_W} |k|^2 \Delta t \right).$$

The parameters of this scheme are: Δt , α , ε , and h . The contour to be detected is given by $\phi = \frac{1}{2}$. Experiments conducted on 3D high-frequency ultrasound medical images have shown that this method is particularly robust to initialization changes [12].

Now, more information is given about the non-parametric estimates used to compute the log-likelihood ratio. As already mentioned, there exists no satisfactory statistical characterization of the sea clutter that can take into account all the various sea states [20]. Dealing with non-parametric estimates avoids making assumptions. Moreover, the computational cost of the Parzen estimation can be significantly reduced in the following way. The initial set of values is divided into subgroups. Then, Parzen estimates are computed from these subgroups. In this paper, a simple uniform subdivision is chosen. Other types of subdivisions can be used according to the application.

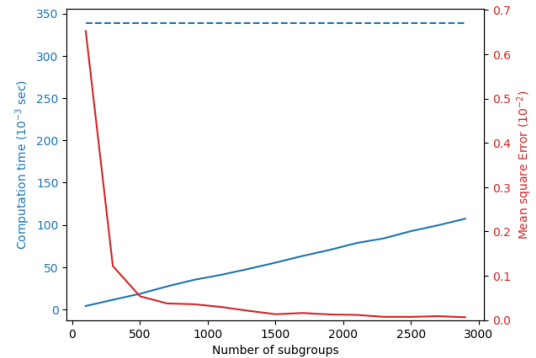


Fig. 1. Evolution of the computational time for the Parzen estimates as a function of the number of subgroups of the initial set. Mean square error appears in red. Initial computational time is $338 \cdot 10^{-3}$ sec.

Fig. 1 illustrates the evolution of the computational time as a function of the number of subgroups for a repeatedly chosen set of $9.5 \cdot 10^3$ values. The mean square error with respect to the estimates computed on the entire set appears in red. For the entire set the computational time is $338 \cdot 10^{-3}$ sec on a standard PC (1.9GHz processor) using a non optimized Python implementation.

C. Chan-Vese k -phase diffuse interface motion

TO allow dealing with an arbitrary number k of phases, it is proposed in [8] to consider the periodic potential \widetilde{W} defined by:

$$\widetilde{W}(x) = W(\langle x \rangle),$$

where W is the double-well potential of (7), and

$$\langle x \rangle = x - [x]$$

where $[x]$ is the largest integer not greater than x . The corresponding Cahn-Hilliard energy writes

$$\widetilde{E}^{CH}(\phi) = \int_{\Omega} \left(\widetilde{W}(\phi(x,t)) + \frac{\varepsilon^2}{2} |\nabla \phi(x,t)|^2 \right) dx.$$

This new energy is the generalization of that given by (6). Dealing with a statistical approach in this multi-phase context is quite more complicated than in the two-phase context. It requires to compute $k > 2$ non-parametric Parzen estimates but also to introduce a relevant dissimilarity measure between these k estimates. This introduces mathematical difficulties in order to obtain the gradient descent and increases the computational cost. Consequently, instead we prefer to constrain the dynamics with an adaptation of the Chan-Vese multi-phase data attachment term introduced in [4] and defined by [8], [10]:

$$\int_{\Omega} G_k(\phi(x,t), \mathcal{I}^N(x)) dx,$$

where \mathcal{I}^N is the normalized image between $[0; 1]$, and

$$G_k(\phi, \mathcal{I}^N) = \frac{\lambda}{2} \sum_{i=0}^k [\mathcal{C}_i - \mathcal{I}^N]^2 \text{sinc}^2(\phi - i).$$

The parameter λ is a regularization coefficient, and \mathcal{C}_i is given by:

$$\mathcal{C}_i = \frac{\int_{\Omega} \mathcal{I}^N(x) \text{sinc}^2(\phi(x,t) - i) dx}{\int_{\Omega} \text{sinc}^2(\phi(x,t) - i) dx}.$$

The multi-grid scheme used is similar to the previous one, see Sec.II-B, with the first step replaced by the minimization of the new data attachment term:

$$\begin{aligned} \phi^n(\bar{x}) \leftarrow \phi^n(\bar{x}) - 2\Delta t \lambda \left[\sum_{i=0}^k [\mathcal{C}_i - \mathcal{I}^N]^2 \frac{\text{sinc}(2[\phi^n(\bar{x}) - i])}{\phi^n(\bar{x}) - i} \right. \\ \left. + \sum_{i=0}^k [\mathcal{C}_i - \mathcal{I}^N]^2 \frac{\text{sinc}^2(\phi^n(\bar{x}) - i)}{\phi^n(\bar{x}) - i} \right]. \end{aligned}$$

The range of values in which the phase-field function evolves is dependent on the number of phases k . Following [8], the initialization is given by:

$$\phi(x,0) = i - 1 + \frac{\mathcal{I}^N(x) - B_{i-1}}{B_i - B_{i-1}}, \quad (8)$$

if $\mathcal{I}^N(x) \in [B_{i-1}, B_i]$, $\forall i = \{1, \dots, k\}$. The values B_i can be adjusted according to the applications at hand (see [25] for details). In the sequel, they are set as

$$B_i = \frac{i}{k}.$$

The parameters of this scheme are: the time step Δt , the number of phases k , the width of the interface ε , and the regularization coefficient λ . The contours to be detected are given by $\phi = i + \frac{1}{2}$, $i \in \{0, \dots, k-1\}$. Due to the nature of the data attachment term, the segmentation tends to produce regions in which the image is piece-wise constant. The transitions between regions are smoothed by the phase-field dynamics.

III. SEA CLUTTER SEGMENTATION

THE most popular approaches to sea clutter segmentation are based on the mathematical modeling of Doppler spectra and are therefore performed in the frequency domain, *i.e.* RDM. Indeed, statistical distributions are designed that aim at describing, from the frequency viewpoint, the superposition of different kinds of waves such as capillary or gravity waves. The current work using CSIR data shows the difficulties in producing relevant geometric segmentation, as illustrated below. Alternatively, one can consider performing segmentation in the initial RTI map without using assumptions about the frequential nature of the sea clutter. RTI maps have characteristics very similar to ultrasound medical images. They are also highly corrupted by the interference noise due to the acquisition mode.

A. Dataset and methodology

THE data used for the experiments come from the CSIR real aperture X-band marine radar campaign 2006–2007 [23]. The radar is located on the coast at 67m above the sea-level. The VV -polarized data is acquired in one sweep mode [17] and contains the following parameters:

- The azimuth angle giving the radar beam direction;

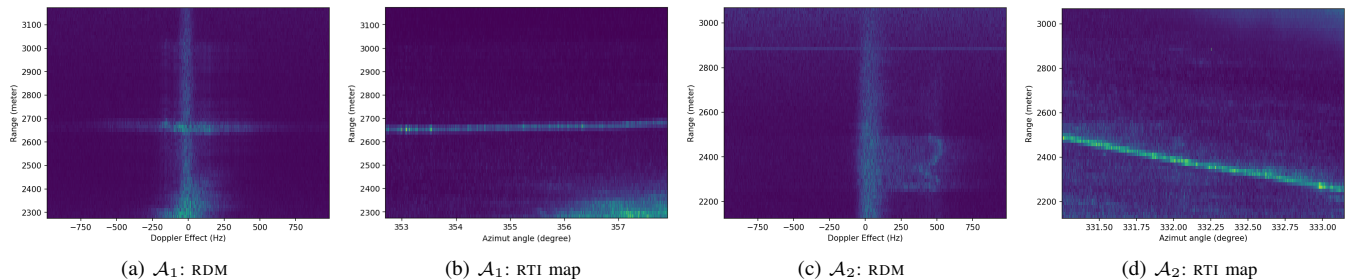


Fig. 2. Range-Doppler and Range-Time Intensity Maps. \mathcal{A}_1 : Douglas sea state 5; target with a tangential motion. \mathcal{A}_2 : Douglas sea state 4.7; target with positive Doppler frequencies.

TABLE I
DESCRIPTION OF THE SELECTED ACQUISITION (RIB DENOTES RIGID
INFLATABLE BOAT)

Name	Size	Douglas sea state	Comments
\mathcal{A}_1	(833, 61, 64)	5	Target (RIB) having a tangential motion (<i>i.e.</i> in endo-clutter) and ground clutter at low range
\mathcal{A}_2	(920, 64, 64)	4.7	Target (RIB) having positive Doppler frequencies (<i>i.e.</i> in exo-clutter) with range side lobes

- The range giving the distance to the radar position;
- The number of pulses grouped in bursts.

Two types of data set described in the Tab. I are used for the evaluation. In the sequel, the complex number (*i.e.* the backscattered signal) after demodulation process is denoted as $\mathcal{A} : (a, r, p) \mapsto \mathcal{A}(a, r, p)$. The triplet (a, r, p) is referred to an azimuth, a range, and a pulse.

There exist two main possibilities to represent these data as grayscale images. The first one is the RTI map that makes use of a non-coherent integration of the backscattered analytic signal (see fig. 2b and 2d):

$$\mathcal{A} : (a, r, \cdot) = (x, \cdot) \mapsto \sum_{i=0}^{p_{\max}} |A(x, i)|, \quad (9)$$

with p_{\max} the number of pulses in each burst. The second one is the RDM, the image obtained in the frequency domain from the entire acquisition (see fig. 2a and 2c which show the slow time *Fourier* transform spectrum plots).

The main purpose of this work is to compare the time and frequency domain sea clutter segmentation results using the three algorithms described in section II. The time domain approach, which is indirect, is proving to be more effective.

For the sake of simplicity, let us denote LS, resp. LL-2P and CV- k P, the algorithms of Sec. II-A, resp. II-B and II-C, and illustrated in fig. 3 to 10. In the figures, the handcrafted ground-truth is given by a red line surrounding the sea clutter.

B. Range-Doppler Map Segmentation

LET us present here the results of the segmentation in the RDM. All the obtained contours for the data \mathcal{A}_1 , resp. \mathcal{A}_2 , are represented in fig. 3, resp. fig. 6.

As a general remark, all the obtained contours are off mark and wider than the real sea clutter. They also contain targets

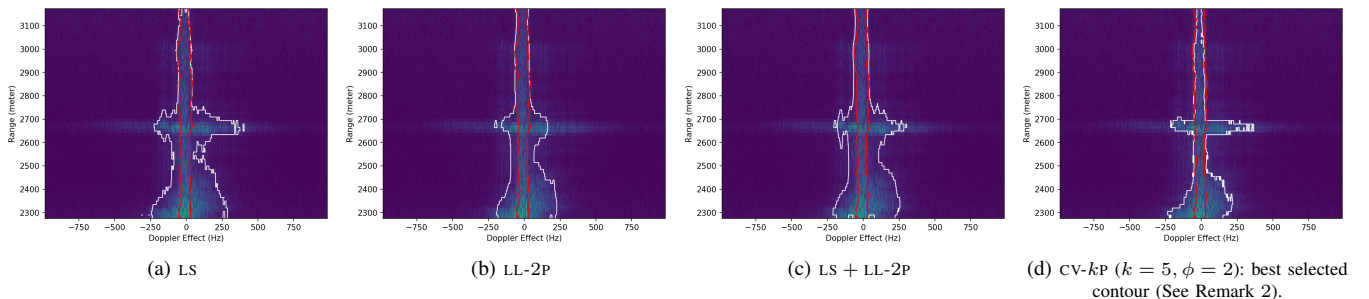


Fig. 3. Segmentation of \mathcal{A}_1 in the RDM – white line for the obtained segmentation and red line for the ground-truth.

with high reflectivity or some ground clutter. Initialization and parameters are chosen as follows:

- The initialization of the LS algorithm is chosen to be equal to 1 on the boundary of the image and equal to -1 everywhere else. Different choices of edge indicator functions give quite similar results. The parameters are set to: $(\Delta t, \mu, \lambda, \sigma, \varepsilon, \alpha) = (3, 0.04, 5, 1, 1.5, 1.5)$. Fig. 3a, resp. fig. 6a shows the result of the segmentation for data \mathcal{A}_1 , resp. \mathcal{A}_2 .

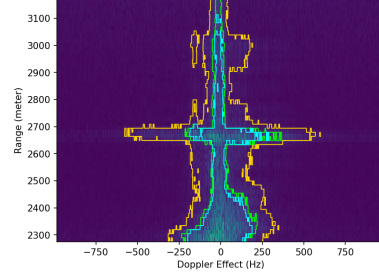


Fig. 4. CV- k P segmentation of \mathcal{A}_1 in the RDM ($k = 5$) – yellow line for $\phi = \frac{1}{2}$, green line for $\phi = \frac{3}{2}$ and cyan line for $\phi = \frac{5}{2}$ (see Remark 2).

- The initialization is trickier for the LL-2P algorithm. This is due to the need to have fairly good initial non-parametric estimates. Therefore, the phase-field function is set to 1 in a vertical band encompassing the vertical line given by the zero Doppler frequency and equal to 0 everywhere else. The parameters are set to: $(\Delta t, a, \varepsilon, h) = (0.1, 6, 1, 0.015)$. Fig. 3b, resp. fig. 6b shows the result of the segmentation for data \mathcal{A}_1 , resp. \mathcal{A}_2 .

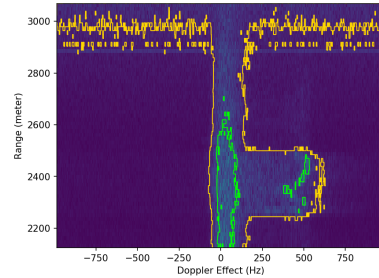


Fig. 5. CV- k P segmentation of \mathcal{A}_2 in the RDM ($k = 4$) – yellow line for $\phi = \frac{1}{2}$ and green line for $\phi = \frac{3}{2}$ (see Remark 2).

- An alternative way that allows avoiding this supervised initialization is to initialize the LL-2P algorithm applying the LS algorithm (denoted LS+LL-2P). Fig. 3c, resp.

(d) CV- k P ($k = 5, \phi = 2$): best selected contour (See Remark 2).

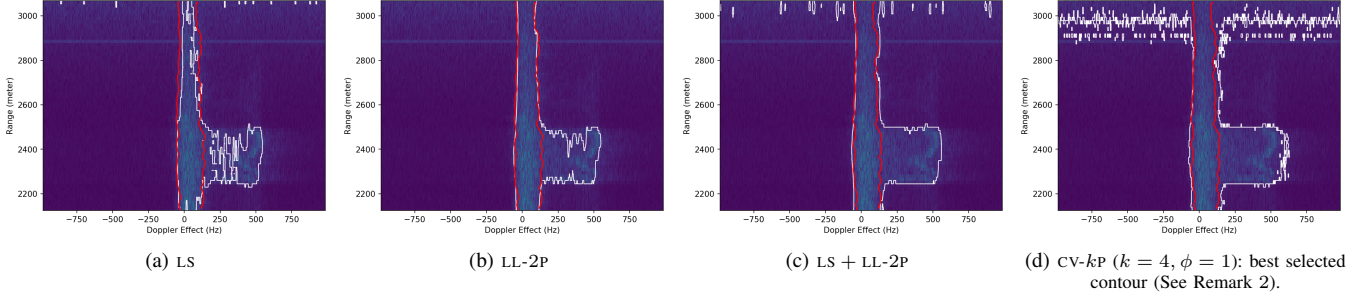


Fig. 6. Segmentation of \mathcal{A}_2 in the RDM – white line for the obtained segmentation and red line for the ground-truth.

fig. 6c, shows the result of the segmentation for data \mathcal{A}_1 , resp. \mathcal{A}_2 .

- The initialization of the CV- kP algorithm is done using (8). The number of phases is set to $k = 5$ and the other parameters are set to: $(\Delta t, \varepsilon, \lambda) = (5 \cdot 10^{-6}, 4 \cdot 10^{-4}, 10)$. Fig. 3d, resp. fig. 6d shows the result of the segmentation for data \mathcal{A}_1 , resp. \mathcal{A}_2 .

Remark 2: For the CV- kP algorithm, all obtained contours are shown in fig. 4, resp. fig. 5, for the data \mathcal{A}_1 , resp. \mathcal{A}_2 . Because of the regularization dynamics, certain phases can be gathered. In order to compare sea clutter segmentation by CV- kP algorithm with that obtained by the other algorithms, the best contour (i.e. the line delimiting two different phases) is shown in fig. 3d, resp. fig. 6d for the data \mathcal{A}_1 , resp. \mathcal{A}_2 .

The early results show clearly that the geometric segmentation algorithms LS, LL-2P and CV- kP are unable to discriminate the frequency information in the RDM to provide a relevant sea clutter segmentation.

C. Range-Time Intensity Map Segmentation with visualization in the Range-Doppler Map

LET us now present the results obtained by considering the second strategy for the sea clutter segmentation. First, the algorithms LS, LL-2P and CV- kP are applied in the RTI

map. Then, the detected contours are visualized in the RDM. Fig. 7 to 10 show the results when this approach is applied to data \mathcal{A}_1 and \mathcal{A}_2 . As illustrated in Fig. 8c and 10c for the data \mathcal{A}_1 and \mathcal{A}_2 , the algorithm CV- kP provides a very good segmentation of the sea clutter.

To exploit the results of the RTI map segmentation and to compare them with those of the previous section, the following process is used. A normalized Parzen estimates $\hat{f}_{h,\mathcal{A}}$ is computed, with $\omega(x) = \phi(x, T_f)$ the phase-field function at the final time evolution T_f . Then, the initial data $\mathcal{A}(x, \cdot)$ is weighted by $\hat{f}_{h,\mathcal{A}}$, i.e.

$$\bar{\mathcal{A}}(x, \cdot) = \hat{f}_{h,\mathcal{A}}(\phi(x, T_f))\mathcal{A}(x, \cdot) \quad (10)$$

Finally, the data $\bar{\mathcal{A}}(x, \cdot)$ is visualized in the RDM (see fig. 8, resp. fig. 10, for the data \mathcal{A}_1 , resp. \mathcal{A}_2). As before, some comments about these further experiments are given.

- The initialization parameters of the LS algorithm are chosen as before. Due to the lack of pronounced contours, edge indicator functions are unable to drive the evolution to produce a meaningful segmentation. There are no relevant edges that could be exploited to isolate the sea clutter. Fig. 8a, resp. fig. 10a, shows the result of the segmentation for data \mathcal{A}_1 , resp. \mathcal{A}_2 .

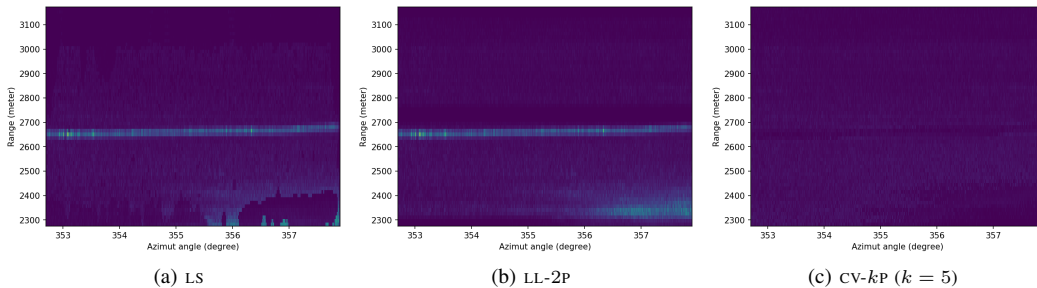


Fig. 7. Visualization of (10) in the RTI map – Data \mathcal{A}_1 .

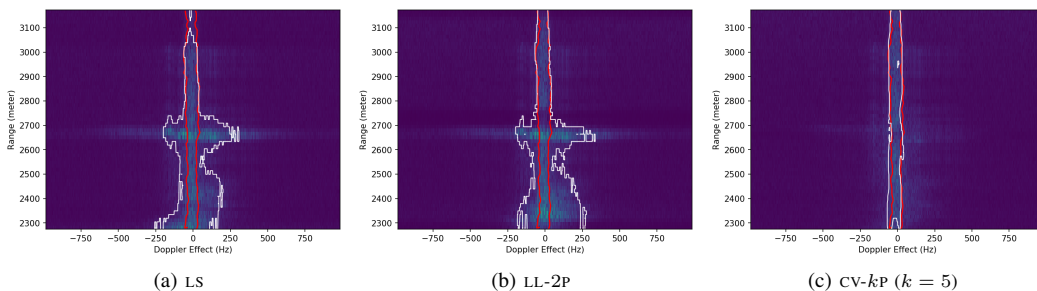
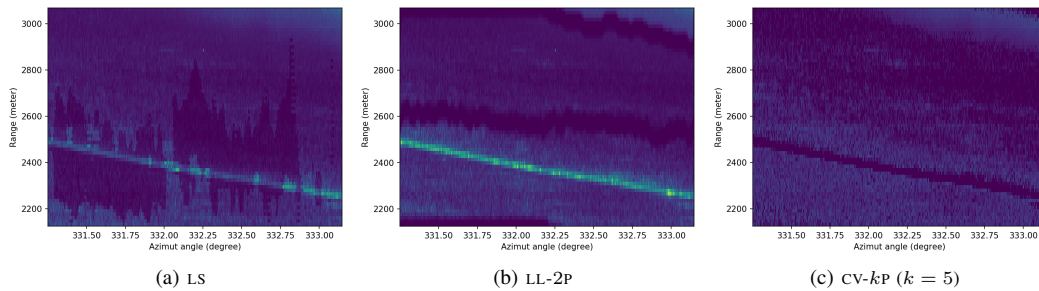
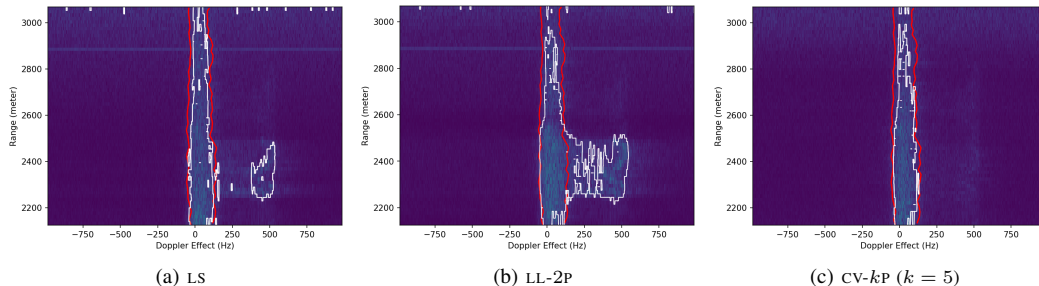


Fig. 8. Visualization of (10) in the RDM – Data \mathcal{A}_1 – white line for the obtained segmentation and red line for the ground-truth.

Fig. 9. Visualization of (10) in the RTI map – Data \mathcal{A}_2 .Fig. 10. Visualization of (10) in the RDM – Data \mathcal{A}_2 – white line for the obtained segmentation and red line for the ground-truth.

- The initialization of the LL-2P algorithm requires more attention than the initialization of the LS algorithm. Hence, an initial contour encompassing a region that is supposed to contain only sea clutter reflectivity is chosen. The parameters are set as in Sec. III-B. This algorithm fails to give a relevant visualization of the sea clutter in the RDM. Hence, the sea clutter can not be discriminated in the RTI map by considering only two classes/phases. Fig. 8b, resp. fig. 10b, shows the result of the segmentation for data \mathcal{A}_1 , resp. \mathcal{A}_2 .
- With the parameters already used in Sec. III-B (apart from the number of phases $k = 8$), the CV- k P algorithm is applied to obtain a phase-field function $\phi(x, T_f)$. The values of $\phi(x, T_f)$ vary between 0 and $k - 1$. Lower values correspond to sea clutter while higher values correspond to high reflectivity items (e.g. ground clutter or target). Fig. 8c, resp. fig. 10c, shows the result of the segmentation for data \mathcal{A}_1 , resp. \mathcal{A}_2 .

D. Assessment and discussion

LET us now discuss in more detail the results of the experiments described in Sec. III-B and III-C. These results cover RDM segmentation and RTI map segmentation with visualization in the RDM. They are obtained for each of the two selected acquisitions: \mathcal{A}_1 and \mathcal{A}_2 . These data have been chosen to be representative of two different situations: high reflectivity target in the endo-clutter and in the exo-clutter. The quality of the segmentation is evaluated based on the proposed ground-truth using the Mean Absolute distance (MAD – for more details, see [12]). This latter aims at measuring how well the boundary of the segmented area corresponds to the ground-truth. The MAD of the various segmentation for \mathcal{A}_1 , resp. \mathcal{A}_2 are reported in Tab. II, resp. Tab. III; recall that the smaller the MAD, the better the segmentation.

– Data \mathcal{A}_1 corresponds to a *Douglas* sea state 5 with a target having a tangential motion with high reflectivity. Such a

target is in the endo-clutter area with near-zero Doppler effect as shown in Fig. 2a. One can also notice ground clutter near-zero frequencies at low range. The Doppler response of the sea clutter and those of potential targets or ground clutter can have great similarities. In fact, at ranges close to 2700m, near-zero frequencies can be assigned to both sea clutter or target. Since without the presence of targets, this region would be part of the sea clutter, it is considered as such for the ground-truth.

Unsurprisingly, and as confirmed by the contours shown in Figure 3 and 6, the three geometric segmentation algorithms fail to discriminate the sea clutter in the RDM. These contours encompass regions corresponding more or less to all significant Doppler frequencies.

Regarding the second approach, the two algorithms LS and LL-2P give comparable results but still far from being satisfactory (see (a) and (b) of fig. 7 and 8). On the contrary, the CV- k P algorithm provides a relevant segmentation (see fig. 8c).

TABLE II
MAD DISTANCE OF SEGMENTATION RESULTS ON DATASET \mathcal{A}_1

	Method	MAD distance
RDM	LS	4.7877
	LL-2P	3.2863
	LS + LL-2P	4.1018
	CV- k P	3.4596
RTI map	LS	3.6513
	LL-2P	3.7744
	CV- k P	0.6778

– Data \mathcal{A}_2 corresponds to a *Douglas* sea state 4.7 with a target having a significant radial speed. Such a target is in the exo-clutter area with Doppler effect higher than the sea clutter Doppler effect as shown in fig. 2c. Visually, the sea clutter and the target appear well separated in the RDM. However, the high speed motion of the target induces waves from wake. Consequently, it induces significant Doppler responses, located between the sea clutter and the target, which are not part of the sea clutter.

Due to the great similarity of the values and gradients of the pixels of interest, none of the three proposed approaches of geometric segmentation in RDM is able to discriminate the sea clutter. It can be seen that there are always some contours encompassing regions containing some high reflectivity target pixels (see fig. 6).

The results given by the alternative approach (segmentation in the RTI map and visualization in the RDM) using LS and LL-2P algorithms are quite similar (see (a) and (b) of fig. 9 and 10). These algorithms still fail to discriminate the sea clutter. On the contrary, when applied with the CV- k P algorithm, this method gives a relevant segmentation (see fig. 10c).

TABLE III
MAD DISTANCE OF SEGMENTATION RESULTS ON DATASET \mathcal{A}_2

	Method	MAD distance
RDM	LS	5.1435
	LL-2P	4.5022
	LS + LL-2P	6.6602
	CV- k P	10.9044
RTI map	LS	5.0306
	LL-2P	5.1867
	CV- k P	1.7139

These results from both data sets \mathcal{A}_1 and \mathcal{A}_2 clearly show the difficulty of identifying the sea clutter in the frequency domain without using some assumptions concerning the existence and/or position of high reflectivity element which are not part of the sea clutter (target, ground clutter. . .). They also show that to be successful, geometric segmentation in the time domain must take into account a much larger number of phases than two.

IV. CONCLUSION

SEA clutter segmentation has been investigated in X-band real aperture marine radar with geometric methods involving interface motions. First, three mathematical models have been described involving sharp or diffuse interfaces and two or more phases. Then, the results obtained by applying these models directly in the RDM and alternatively in the RTI map with visualization in the RDM have been compared. Experiments have been conducted on real coherent radar images with sea states 4.7 and 5.

Our approach differs from most conventional methods since it relies on geometric algorithms of image processing that do not involve assumptions on the nature of the sea clutter or statistical models. Dealing with the reflectivity information of RTI maps obtained by non-coherent integration does not allow to investigate the presence of potential targets with lower reflectivity than the sea clutter. In consequent, the proposed algorithm can be considered as a simple, efficient and unsupervised tool to obtain for instance oceanographic parameters or for further investigation regarding target detection by means, for instance, of learning methods.

ACKNOWLEDGMENT

This work is partially supported by the French Defense Innovation Agency. We thank the CSIR for access to the small boat trails sea-clutter database.

REFERENCES

- [1] S. M. Allen and J. W. Cahn, "A microscopic theory for antiphase boundary motion and its application to antiphase domain coarsening," *Acta metallurgica*, vol. 27, no. 6, pp. 1085–1095, 1979. [Online]. Available: <https://www.sciencedirect.com/science/article/pii/0001616079901962>.
- [2] G. Avinash and B. Deepashree M., "Image segmentation using distance regularized level set method," *International Journal of Advanced Research in Electronics and Communication Engineering*, vol. 5, no. 2, pp. 262–267, 2016. [Online]. Available: <http://dl.icdst.org/pdfs/files/3/325c3b5cbee093b6ca80d047c45b54c7.pdf>.
- [3] E. Bretin, *Mouvements par courbure moyenne et méthode de champs de phase*. PhD thesis, Institut National Polytechnique de Grenoble (INPG), 2009. [Online]. Available: https://tel.archives-ouvertes.fr/file/index/docid/995323/filename/these_bretin_elie.pdf.
- [4] T. F. Chan and L. A. Vese, "Active contours without edges," *IEEE Transactions on Image Processing*, vol. 10, no. 2, pp. 266–277, 2001. [Online]. Available: <https://ieeexplore.ieee.org/document/902291>.
- [5] V. C. Chen, F. Li, S.-S. Ho, and H. Wechsler, "Micro-Doppler effect in radar: phenomenon, model, and simulation study," *IEEE Transactions on Aerospace and Electronic Systems*, vol. 42, no. 1, pp. 2–21, 2006. [Online]. Available: <https://ieeexplore.ieee.org/document/1603402>.
- [6] S. Kemkemian and V. Corretja, "A new adaptive CA-CFAR based on local topology of sea clutter for coherent detection in high sea state," in *2019 20th International Radar Symposium (IRS)*, pp. 1–9, IEEE, jun 2019. [Online]. Available: <https://ieeexplore.ieee.org/document/8768167>.
- [7] C. Li, C. Xu, C. Gui, and M. D. Fox, "Distance regularized level set evolution and its application to image segmentation," *IEEE Transactions on Image Processing*, vol. 19, no. 12, pp. 3243–3254, 2010. [Online]. Available: <https://ieeexplore.ieee.org/document/5557813>.
- [8] Y. Li and J. Kim, "Multiphase image segmentation using a phase-field model," *Computers & Mathematics with Applications*, vol. 62, no. 2, pp. 737–745, 2011. [Online]. Available: <https://www.sciencedirect.com/science/article/pii/S0898122111004652>.
- [9] Y. Li, W. Zeng, N. Zhang, and W. Tang, "Gabor feature based ionospheric clutter region extraction in Range-Doppler Map," in *2014 IEEE Antennas and Propagation Society International Symposium (APSURSI)*, pp. 269–270, IEEE, 2014. [Online]. Available: <https://ieeexplore.ieee.org/document/6904466>.
- [10] S. Liu and Y. Peng, "A local region-based Chan–Vese model for image segmentation," *Pattern Recognition*, vol. 45, pp. 2769–2779, jul 2012. [Online]. Available: <https://www.sciencedirect.com/science/article/pii/S0031320311004717?via%3Dihub>.
- [11] C. Mantegazza, *Lecture notes on mean curvature flow*, vol. 290. Springer Science & Business Media, 2011.
- [12] K. L. Nguyen, P. Delachartre, and M. Berthier, "Multi-grid phase field skin tumor segmentation in 3D ultrasound images," *IEEE Transactions on Image Processing*, vol. 28, no. 8, pp. 3678–3687, 2019. [Online]. Available: <https://ieeexplore.ieee.org/document/8648477>.
- [13] S. Osher and J. A. Sethian, "Fronts propagating with curvature-dependent speed: algorithms based on Hamilton–Jacobi formulations," *Journal of computational physics*, vol. 79, no. 1, pp. 12–49, 1988. [Online]. Available: <https://www.sciencedirect.com/science/article/pii/0021999188900022?via%3Dihub>.
- [14] M. Parenthoën, T. Jourdan, and J. Tisseau, "IPAS: Interactive Phenomenological Animation of the Sea," 2004. [Online]. Available: <https://hal.archives-ouvertes.fr/hal-01170245/document>.
- [15] E. Parzen, "On estimation of a probability density function and mode," *The annals of mathematical statistics*, vol. 33, no. 3, pp. 1065–1076, 1962. [Online]. Available: <https://projecteuclid.org/euclid.aoms/1177704472>.
- [16] A. M. Raynal and A. W. Doerry, "Doppler characteristics of sea clutter," *New Mexico: Sandia National Laboratories*, jun 2010. [Online]. Available: <https://prod-ng.sandia.gov/techlib-noauth/access-control.cgi/2010/103828.pdf>.
- [17] M. I. Skolnik, "Radar handbook, third edition," *Mc Graw-Hill Companies*, 2008.
- [18] M. Stempel, J. P. De Villiers, J. E. Cilliers, and A. McDonald, "Distribution analysis of segmented wave sea clutter in littoral environments," in *2015 IEEE Radar Conference*, pp. 133–138, IEEE, oct 2015. [Online]. Available: <https://ieeexplore.ieee.org/document/7411868>.
- [19] D. Tao, A. P. Douglgeris, and C. Brekke, "A segmentation-based CFAR detection algorithm using truncated statistics," *IEEE Transactions on Geoscience and Remote Sensing*, vol. 54, no. 5, pp. 2887–2898, 2016. [Online]. Available: <https://ieeexplore.ieee.org/document/7384481>.

- [20] F. Totir, E. Radoi, L. Anton, C. Ioana, A. Serbanescu, and S. Stankovic, "Advanced sea clutter models and their usefulness for target detection," *MTA Review*, vol. 18, no. 3, pp. 257–272, 2008. [Online]. Available: <https://hal.archives-ouvertes.fr/hal-00349339/document>.
- [21] D. Walker, "Doppler modelling of radar sea clutter," *IEE Proceedings-Radar, Sonar and Navigation*, vol. 148, no. 2, pp. 73–80, 2001. [Online]. Available: https://digital-library.theiet.org/content/journals/10.1049/ip-rsn_20010182.
- [22] S. Watts, "Modeling and simulation of coherent sea clutter," *IEEE Transactions on Aerospace and Electronic Systems*, vol. 48, no. 4, pp. 3303–3317, 2012. [Online]. Available: <https://ieeexplore.ieee.org/document/6324707?denied=>.
- [23] H. De Wind, J. Cilliers, and P. Herselman, "Dataware: Sea clutter and small boat radar reflectivity databases [best of the web]," *IEEE Signal Processing Magazine*, vol. 27, no. 2, pp. 145–148, 2010. [Online]. Available: <https://ieeexplore.ieee.org/document/5438949>.
- [24] T. Wu, Z. Luo, Z. He, W. Zhaoyi, and X. Chen, "Sea-clutter region extraction based on image segmentation methods for over-the-horizon radar," in *2018 IEEE Radar Conference (RadarConf18)*, pp. 389–393, IEEE, 2018. [Online]. Available: <https://ieeexplore.ieee.org/document/8378590>.
- [25] Y. Yang, Y. Zhao, B. Wu, and H. Wang, "A fast multiphase image segmentation model for gray images," *Computers & Mathematics with Applications*, vol. 67, pp. 1559–1581, may 2014. [Online]. Available: <https://www.sciencedirect.com/science/article/pii/S0898122114000418>.



Michel Berthier received in Ph.D. degree in mathematics at the University of Dijon (France) in 1993 and his "Habilitation à Diriger des Recherches" in mathematics at the University of Rennes (France) in 1999. He worked as a French CNRS researcher between 1993 and 1999 and is currently full professor of mathematics at the University of La Rochelle (France). His main interests are differential and *Riemannian* geometry, and *Clifford* and *Jordan* algebras applied to image processing and understanding.



Jordan Michelet received the Master's degree in Applied Mathematics, Signal and Image Processing from La Rochelle University (France) in 2019. He is currently a Ph.D. student in the Mathematics Image and Applications Laboratory in La Rochelle University (France). His doctoral is both supported by ERTÉ-ETSA Bowen group from Paris and the French Defense Innovation Agency (France). His research interests include radar signal processing and analytic/monogenic signal.



Laurent Mascarella received his Ph.D. in Computer Science from the University of Toulouse III (France) in 1996 and his "Habilitation à Diriger des Recherches" in computer science from La Rochelle University (France) in 2008. He is currently associate professor in the Mathematics Image and Applications Laboratory in La Rochelle University (France). His research interests include image processing, video analysis and machine learning.

Henry Chandran graduated from Oxford Brookes University, UK, in 1982. He has broad experience in knowledge-based signal processing for severe environments and its implementation in digital and radio-frequency hardware. His technical collaboration includes various research programs at national and European level. He is currently working as a consultant in the field of knowledge-based marine radar systems for high seas states.